Journal of *Marine Science and Engineering*

MDPI

Article

Machine Learning Combined with Numerical Simulations: An Effective Way to Reconstruct the Detonation Point of Contact Underwater Explosions with Seabed Reflection

Jacopo Bardiani [1], Giada Kyaw Oo D'Amore [2], Claudio Sbarufatti [1,*] and Andrea Manes [1]

[1] Department of Mechanical Engineering, Politecnico di Milano, Via G. La Masa 1, 20156 Milano, Italy; jacopo.bardiani@polimi.it (J.B.); andrea.manes@polimi.it (A.M.)
[2] Department of Engineering and Architecture, University of Trieste, Via A. Valerio 6, 34127 Trieste, Italy; giada.kyawood'amore@dia.units.it
* Correspondence: claudio.sbarufatti@polimi.it

Abstract: In marine engineering, the study of underwater explosion effects on naval and offshore structures has gained significant attention due to its critical impact on structural integrity and safety. In practical applications, a crucial aspect is determining the precise point at which an underwater explosive charge has detonated. This information is vital for assessing damage, implementing defensive and security strategies, and ensuring the structural integrity of marine structures. This paper presents a novel approach that combines coupled numerical simulations performed using the MSC Dytran suite with machine learning techniques to reconstruct the trigger point of underwater explosions based on onboard sensor data and leverage seabed wave reflection information. A Multi-Layer Neural Network (MLNN) was devised to identify the position of the denotation point of the charge using a classification task based on a user-defined two-dimensional grid of potential triggering locations. The MLNN underwent training, validation, and testing phases using simulation data from different underwater blast-loading scenarios for metallic target plates. Different positions of the charge, seabed typologies, and distances between the structure and the seabed are considered. The ability to accurately identify a detonation point using measurable data from onboard systems enhances the knowledge of ship and offshore structures' response strategies and the overall safety of naval operations.

Keywords: underwater explosion; fluid-structure interaction; machine learning; multi-layer neural network; seabed reflection; onboard sensors

Academic Editors: Fausto Pedro García Márquez and Coro Gianpaolo

Received: 14 February 2025
Revised: 27 February 2025
Accepted: 5 March 2025
Published: 9 March 2025

Citation: Bardiani, J.; Kyaw Oo D'Amore, G.; Sbarufatti, C.; Manes, A. Machine Learning Combined with Numerical Simulations: An Effective Way to Reconstruct the Detonation Point of Contact Underwater Explosions with Seabed Reflection. *J. Mar. Sci. Eng.* **2025**, *13*, 526. https://doi.org/10.3390/jmse13030526

1. Introduction

Understanding the dynamic behaviour of floating and submerged structures under pressure loads is vital for the naval shipbuilding and offshore engineering industries. Underwater explosions (UNDEXs) are especially important among the different sources of pressure loads, as they directly affect the safety and performance of underwater vehicles (like submarines) and various marine structures (such as drilling platforms, cargo ships, and warships) [1–3].

A typical UNDEX event can induce three separate damaging mechanisms in a marine structure, depending on the distance from the hull [4–6]; initially, primary shock waves hit the hull with high velocity and pressure. Following this, lower-frequency pressure waves, resulting from the pulsation of the gas bubbles produced by the explosion, excite the structure. Lastly, the collapse of these gas bubbles generates high-speed water jets that can impact the target structure.

The three mechanisms described above lead to highly complex phenomena due to fluid–structure interaction (FSI), significant deformations and fracturing, and material non-linearity influenced by high strain rates and temperatures [7–9]. In fact, the FSI caused by UNDEX events can result in several interconnected effects, such as cavitation, wave reflection, and energy absorption [10].

Based on whether the structure falls within the bubble's impact zone, UNDEXs can be classified as either non-contact or contact explosions [11]. Non-contact explosions are further divided into far-field and near-field explosions, depending on the stand-off distance. In far-field UNDEXs, the stand-off distance exceeds the maximum radius of the bubbles formed during the first pulsation [12,13].

There are three main methodologies employed to study UNDEXs and their impacts on marine structures: experimental tests, analytical models, and numerical simulations [1].

Experimental studies are challenging due to the complex and hazardous nature of UNDEXs [11,14]. Additionally, high costs and logistical difficulties make these experiments particularly prohibitive, especially for full-scale tests [15,16]. While scaled specimens offer a useful approximation, the publication of experimental data is infrequent, hindering a comprehensive understanding of UNDEX phenomena [17].

Analytical models play a crucial role in studying UNDEX events, offering a theoretical framework to understand potential effects and outcomes. However, these models often fall short due to their simplifications and approximations, which may not adequately represent the complexity of real-world phenomena [1,4,18].

Given these challenges, significant advancements in numerical methods and computing performance have enabled effective numerical simulations of UNDEX events on high-performance computers [16]. Advanced software such as LS-DYNA, ABAQUS, ANSYS, and MSC Dytran is widely used to predict the transient loading and structural responses of various marine structures [14,17].

Numerical approaches to simulating UNDEXs can be broadly categorised into coupled and decoupled methodologies. Coupled methodologies address the interaction between the explosion-induced pressure wave and the dynamic response of the ship's hull within a unified computational framework, allowing for simultaneous solutions [19,20]. In contrast, decoupled methodologies do not directly simulate FSI, and they tackle the fluid and structural domains separately in two distinct steps [21,22]. It is commonly noted that coupled models tend to be the most accurate because they closely represent the physical processes involved. In contrast, decoupled models are typically more efficient, require fewer computing resources, and are simpler to implement [22].

Coupled numerical approaches used to investigate transient FSI issues in UNDEX scenarios can be categorised into three main types based on the methods applied to model the fluid and structural domains [23]: Eulerian–Eulerian (E–E), Lagrangian–Lagrangian (L–L), and Eulerian-Lagrangian (E–L). The most utilised technique for modelling FSI is the coupled Eulerian-Lagrangian (CEL) method. The CEL approach leverages the advantages of Eulerian theory for fluid modelling and Lagrangian theory for structural modelling, facilitating continuous interaction between the two [24].

Despite extensive research into the dynamic responses of ship hulls and offshore structures under UNDEX loading, coupled methods such as CEL are still limited by their high computational cost [1,17]. Naval platforms have big dimensions and require large Eulerian volumes to accurately model the water around them, resulting in a huge number of cells. Moreover, the complex algorithms needed to handle the interface and interaction between the Eulerian and Lagrangian phases pose additional computational challenges.

The computational demands and time required to run such simulations make them impractical for providing immediate feedback or data, which is crucial in real-time usage

during operational scenarios regarding marine structures. For that reason, the necessity of tools that make quick predictions regarding UNDEX effects on marine structures is imperative.

The integration of machine learning (ML) techniques into this framework offers a powerful and innovative solution to achieve this goal [1,25]. ML methods can reveal complex relationships between inputs and outputs by analysing extensive datasets of intricate phenomena through a comprehensive training process, allowing computers to learn from past experiences without explicit programming [26].

Nevertheless, only a few studies have utilised ML in the context of UNDEXs. For example, Refs. [9,17] employed a deep neural network (DNN) to forecast the dynamic response of reinforced plates exposed to near-field UNDEXs, testing various charge masses, stand-off distances, and plate thicknesses. Additionally, Ref. [27] used DNNs to predict the structural response of reinforced cylindrical shells subjected to far-field UNDEXs based on numerical simulation results. In Ref. [25], a multi-layer perceptron-based neural network was combined with a multiscale finite element method to estimate the structural response of a coated composite cylinder under near-field UNDEXs.

Despite the previous examples, which have already provided evidence that machine learning techniques can be leveraged to deal with UNDEXs against submerged and floating marine structures, one underexplored aspect is the development of tools that enable the reconstruction of critical features relevant to practical onboard applications.

The novel idea of the present work concerns the implementation of a framework for practical applications, in which the detonation point of an underwater explosive is reconstructed using various sources of information—some known to the ship's crew and others obtained from sensors or instrumentation placed on the hull structure. To achieve this goal, numerical simulations are employed alongside a machine learning model capable of capturing complex input–output relationships. Currently, no existing frameworks can provide actionable information immediately after events such as UNDEXs, making our approach particularly relevant for real-world use.

In fact, determining the precise location of an underwater explosive charge is critical for military and civilian vessels, as well as offshore structures, because it allows for an accurate assessment of potential damage to naval vessels or offshore structures, enabling timely and effective countermeasures to protect these valuable assets and ensure operational safety.

In particular, the information needed as input to the Multi-Layer Neural Network (MLNN) to achieve the goal of the paper regards the following: the material that characterises the target structure, the type of seabed, the distance between the seabed and the structure, the initial value of the mass-per-unit-area of the target, the pressure-time history recorded at a specific point on the structure, and the out-of-plane displacement-time history registered from the same point where the pressure is measured.

The classification task performed by the MLNN is applied (for simplicity) to a user-defined two-dimensional grid, equally spaced in both directions, where each class in the output represents a specific detonation point where the charge is ignited. The output of the MLNN is represented by the probability that the charge exploded at a specific point in the user-defined grid.

Given the high computational cost of underwater explosion analysis on real ship structures, the framework was implemented using a simple, submerged square plate positioned horizontally and fully clamped along the four sides.

The paper is organised as follows: in Section 2, the entire framework is described in detail, focusing on the numerical simulations' dataset and the adopted machine learning algorithm. MSC Dytran 2024.1 version was used for numerical calculations, and the results were assessed against the experimental results reported in [28]. Section 3 presents and

discusses the obtained results. Finally, the conclusions are summarised, highlighting the advantages and drawbacks of the adopted methodology, and future enhancements and developments are proposed.

2. Methodology

The proposed data-driven framework for contact UNDEX scenarios is composed of the following steps:

1. **Numerical simulations**: Simulations of horizontal, fully clamped, underwater blast-loaded plates were carried out to generate the dataset for the data-driven approach. The validation of the simulations against an experimental case scenario is described in Section 2.1.1. Various scenarios were considered, involving different loading conditions and plate and seabed characteristics. The CEL approach is employed in all simulations, ensuring the consideration of fluid–structure interaction (FSI).
2. **Dataset generation**: All numerical simulations were post-processed using ParaView [29] to extract the data necessary to build the MLNN. Data were extracted both for the fluid and for the structural domains (plate and seabed). The considered structural parameters are the plate out-of-plane displacement, initial mass-per-unit-area, elastic modulus of the plate and seabed, vertical distance between the plate and the seabed, and finally, the position of the charge within the user-defined grid. For the fluid domain, the fluid pressure at the central point of the plate is the only parameter considered.
3. **Data-driven approach**: A Multi-Layer Neural Network (MLNN) was developed to classify a generic explosive event under the plate into one of several classes, where each class corresponds to a specific position in the charge's spatial configuration (user-defined bidimensional grid). The MLNN is implemented using the PyTorch 2.5.0 library in Python 3.13.0. Training, validation, and testing are performed on the numerical dataset, as outlined below:
    - Throughout training and validation, the MLNN learns how to correlate input parameters from each explosive scenario to the specific class, i.e., reconstruct the position of the explosive detonation point;
    - After training, the MLNN is tested against the unseen scenarios included in the testing split to verify its generalisation capabilities.

    Each part of the present framework is described in detail in the following paragraphs.

2.1. Numerical Simulations

2.1.1. Validation of the Numerical Framework

Due to the challenges in reproducing UNDEX experimental tests, a literature case study was used to assess the numerical model developed in MSC Dytran. In particular, the experimental investigation proposed by Ramajeyathilagam et al. is considered [28], where rectangular, unstiffened steel plates with exposed areas of 0.30×0.25 m^2 were subjected to underwater shock. To avoid overburdening the discussion, only a comparison of the numerical and experimental results is presented in Figure 1, highlighting a strong agreement, with a maximum error between the numerical model and experimental evidence of less than 3%. For further details on the experimental trial, refer to [28]. The mesh size considered in the present model is 5 mm.

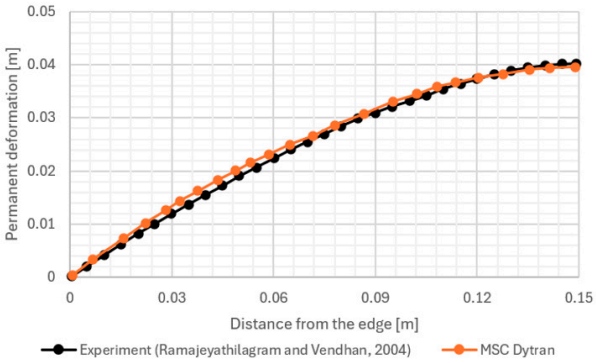

Figure 1. Comparison of the numerical and the experimental results regarding the centreline deformation profile [28].

2.1.2. Numerical Simulations of the Dataset

All numerical simulations are performed using MSC Dytran version 2023.3, which is an explicit finite element analysis (FEA) solver for the simulation of short-lived events, such as shocks and collisions, and the analysis of the complex non-linear behaviour that structures undergo during these events. MSC Patran version 2023.3 was used to discretise geometries and generate the Eulerian mesh.

Horizontal fully clamped plates, alternatively made using aluminium or steel, are simulated under different contact underwater explosion loadings according to the schematic representation presented in Figure 2 (non-scaled drawing).

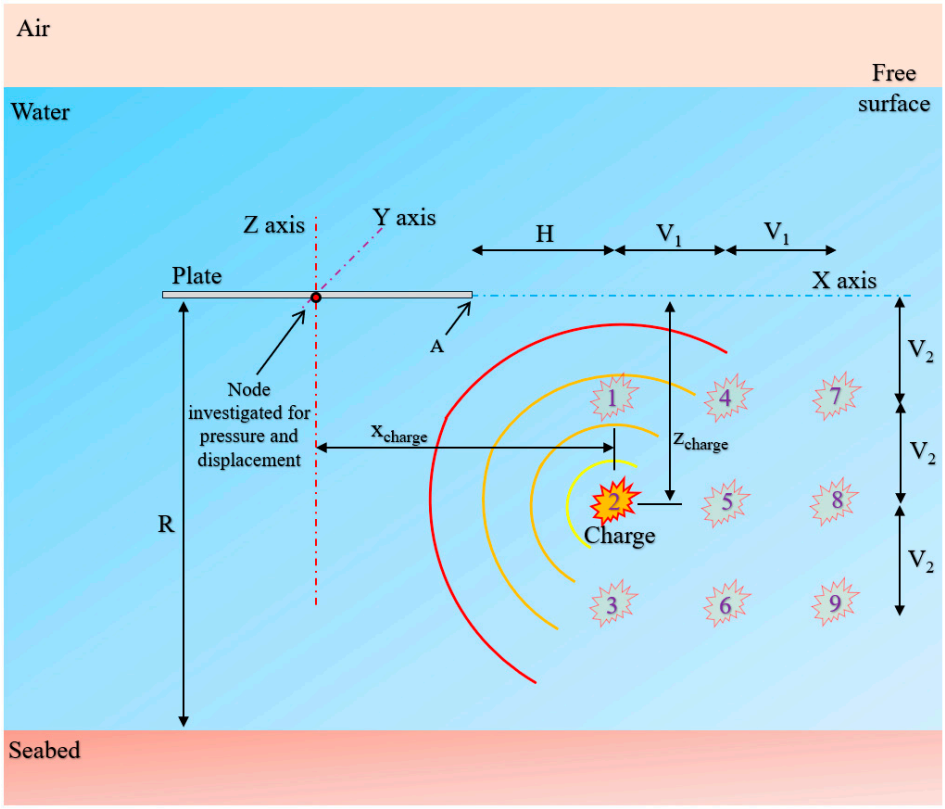

Figure 2. Scenarios considered: relative position between structure and charge.

All squared plates have an exposed area of 500 mm × 500 mm, with the same thickness equal to 5 mm. The geometric centre of the horizontal plates was fixed 2 m below the free surface. Although contact explosions are considered in the study, it should be noted that the behaviour of the gas bubble is not considered, and all analyses are stopped before the

gas bubble touches the structure. This assumption does not compromise the framework and the validity of the results, aiming at identifying the location of the explosion. For such purposes, the framework takes information (e.g., pressure and displacement) in a time step before the starting of gas bubble phenomena. Several UNDEX scenarios were simulated, considering different materials for the plate, type of seabed, distance between the seabed and the structure (called R), and final position of the charge within the user-defined two-dimensional grid reported in Figure 2. The grid is characterised by the constant values $H = 0.40$ m, $V_1 = 0.20$ m, and $V_2 = 0.20$ m. Two values of R have been considered: 0.9 m (signed as $R1$) and 1.1 m (signed as $R2$). V_1 represents the horizontal distance, measured along the X-axis of Figure 2, between point A of the structure (Figure 3a) and the centre of the explosive charge. V_2 represents the same distance but is measured along the vertical Z-axis. Conversely, H is the horizontal distance between point A and the centre of the explosive charge closest to the structure. H, V_1, and V_2 allow for the unique identification of the spacing of the two-dimensional grid and its position with respect to the structure under examination.

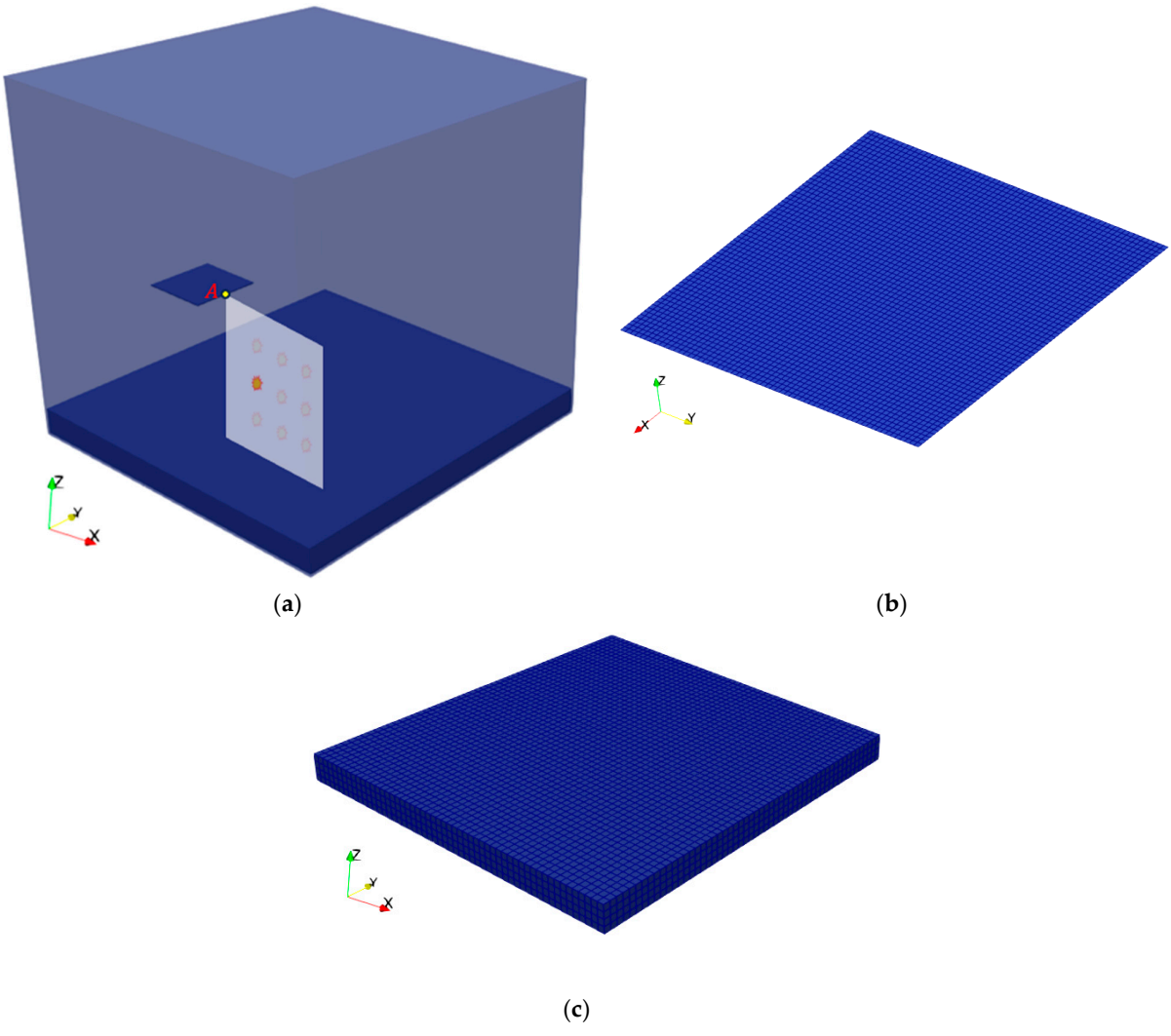

Figure 3. (**a**) The 3-D numerical model considered for non-contact UNDEXs; (**b**) fully clamped plate with its mesh, and (**c**) the solid representing the seabed with full clamps on the bottom surface.

The explosion load cases are reported in Table 1, including the code, type, and mass of the charge (TNT, $m = 1.47$ [kg]), the equation of state used to numerically model the charge (for all cases Jones-Wilkins-Lee equation, JWL), the radius of the charge's sphere,

R_{charge}, the Keel Shock Factor (KSF), and finally, the coordinate of the charge with respect to the reference system of Figure 2 (x_{charge} and z_{charge}).

Table 1. Features of the explosion scenarios considered.

Code	Charge	m [kg]	EOS	R_{charge} [m]	x_{charge} [m]	z_{charge} [m]	KSF [−]
LC1	TNT	1.47	JWL	0.060	0.65	0.20	1.95
LC2	TNT	1.47	JWL	0.060	0.65	0.40	1.81
LC3	TNT	1.47	JWL	0.060	0.65	0.60	1.53
LC4	TNT	1.47	JWL	0.060	0.85	0.20	1.25
LC5	TNT	1.47	JWL	0.060	0.85	0.40	1.31
LC6	TNT	1.47	JWL	0.060	0.85	0.60	1.21
LC7	TNT	1.47	JWL	0.060	1.05	0.20	0.91
LC8	TNT	1.47	JWL	0.060	1.05	0.40	0.99
LC9	TNT	1.47	JWL	0.060	1.05	0.60	0.97

As mentioned before, all simulations belong to contact UNDEXs despite the framework being independent of this classification. To verify it, the authors calculated the maximum radius of gas bubbles arising from the explosions to compare it with the distance from the structure, according to the formulation reported in [30,31]:

$$r_{b,max} = \left(K_6 \cdot W^{1/3}\right) / \left(\overline{D} + 9.8\right)^{1/3} \quad (1)$$

In the above equation, $r_{b,max}$ is the maximum bubble radius, W is the weight of the charge in kg (TNT equivalent), $\overline{D}$ is the depth of charge in water in meters, and finally, K_6 is a constant proper of the given type of explosive (for TNT, 3.383 $\left[\mathrm{m}^{4/3}/\mathrm{kg}^{1/3}\right]$). Considering, for instance, the charge located in position 9 of Figure 2, Equation (1) provides a value of the maximum bubble radius equal to 1.66 [m], considering $\overline{D} = 2 + 3 \cdot V$. Since $r_{b,max}$ is greater than the distance between the centre of the charge and the first point of the structure reached by the shock (1.00 [m]), this case belongs to contact type. The same consideration is valid for all the other scenarios.

Table 1 provides information about the Keel Shock Factor (KSF), which can be considered the index of explosion severity regarding the damage suffered by components mounted inside the hull, for example, on decks and bulkheads. It is computed using the following [32]:

$$KSF = \sqrt{W}/D \cdot (1 + sin\alpha)/2 \quad (2)$$

where W is the weight of the charge in kg, D is the minimum distance in meters between the centre of the charge and the hull, and α represents the angle between the vertical passing through the keel point and the line joining that point with the centre of the charge. For the plates under examination, the first point of the plate closest to the charge is considered.

All load cases in Table 1 refer to the detonation point located in the same plane with Y-normal, moving through the central point of the plate under examination.

As far as the 3-D numerical model is concerned, the Lagrangian domain is split into two portions, represented by the plate and the seabed (Figure 3). The plates are represented using Lagrangian quadrilateral shell elements with a base size of 8 mm (Figure 3b). The chosen mesh size was determined based on a mesh convergence analysis, which demonstrated that further refinement did not significantly affect the out-of-plane displacement of the plate. For simplicity, the details of this analysis are not reported here. The physical properties of the two materials considered for the plates are shown in Table 2. Both steel

and aluminium plates have been considered since they are the most used in the naval sector [33].

Table 2. Physical constants of the plate materials used in the numerical simulations.

Material	Code	E_{plate} [GPa]	ν [−]	ρ [kg/m^3]
6061-T6	ST	210.0	0.33	7850
AISI-316L	AL	70.0	0.30	2700

All plate materials considered are governed by the von Mises criterion, according to the Johnson–Cook plasticity model, in which the equivalent yield stress, σ_Y, is expressed as

$$\sigma_Y = \left[A + B \cdot \left(\varepsilon_e^{pl}\right)^n\right] \cdot \left[1 + C \cdot \ln\left(\frac{\dot{\varepsilon}_e^{pl}}{\dot{\varepsilon}_0}\right)\right] \cdot \left[1 - \left(\frac{T - T_{ROOM}}{T_M - T_{ROOM}}\right)^m\right] \quad (3)$$

where A is the yield stress, B is the strain-hardening coefficient, ε_e^{pl} is the equivalent or effective plastic strain, n is the strain-hardening index, C is the strain-rate parameter, $\dot{\varepsilon}_0$ is the reference strain rate (measured per unit time), $\dot{\varepsilon}_e^{pl}$ is the equivalent plastic strain rate, T is the actual temperature, T_{ROOM} is the room temperature, T_M is the melting temperature, and finally, m is the thermal softening coefficient. All the parameters considered for the two materials are reported in Table 3.

Table 3. Material parameters of the plate materials used in the numerical simulations.

Alloy	A [MPa]	B [MPa]	n [−]	C [−]	$\dot{\varepsilon}_0$ [s^{-1}]	m [−]	Ref.
6061-T6	270.0	154.30	0.221	0.130	1.0	1.34	[1]
AISI-316L	490.0	600.00	0.210	0.015	1.0	0.60	[1,8]

For a complete high-fidelity representation of the progressive damage of the structure under the underwater blast event, structural damage behaviour is considered using the Johnson–Cook failure model. It defines the properties of a failure model, where failure is determined by a damage model. The damage model is given by the following expressions:

$$\varepsilon_{frac} = \left[D_1 + D_2 \cdot e^{D_3 \cdot \sigma^*}\right] \cdot \left[1 + D_4 \cdot \ln\left(\dot{\varepsilon}_{pl} / \dot{\varepsilon}_{pl}^0\right)\right] \cdot \left[1 + D_5 \cdot \frac{T - T_{ROOM}}{T_M - T_{ROOM}}\right] \quad (4)$$
$$\sigma^* = p/q$$

where ε_{frac} is the equivalent plastic strain at the onset of damage, $D_1 - D_5$ are failure parameters, p is the mean (or hydrostatic) stress, q is the von Mises stress, $\dot{\varepsilon}_{pl}^0$ is the reference strain rate, and $\dot{\varepsilon}_{pl}$ is the plastic strain rate. T, T_{ROOM}, and T_M have already been defined above. In this study, the effect of temperature on structure response is not considered due to the adiabaticity of blast wave interaction and only the first two terms of the equation are implemented. The values of the parameters of the Johnson–Cook damage model for the materials used are reported in Table 4:

Table 4. Identification of the parameters of the steel and aluminium used within the Johnson-Cook failure model.

Mat.	D_1 [MPa]	D_2 [MPa]	D_3 [−]	D_4 [−]	D_5 [−]	$\dot{\varepsilon}_{ref}$ [−]	Ref.
6061-T6	0.025	16.93	−14.8	0.0214	0	1.0	[1]
AISI-316L	0.096	0.049	−3.46	0.0160	0	1.0	[1,8]

For the solid that represents the seabed portion, Lagrangian hexahedron solid elements with a base size of 15 mm were used (Figure 3c). Three types of soil were considered, and the Mohr-Coulomb yield model was used for modelling [34]. The material property values of the seabed required for the numerical simulation are estimated by referring to the existing research results and the detailed property values, which were put in order and are shown in Table 5.

Table 5. Material properties for the different soils of the seabed (values taken from [35]).

Material	Code	E_{seabed} [Pa]	ν [−]	ρ [kg/m^3]	c' [Pa]	ϕ [°]	Shear Strength [Pa]
Sand	SB1	10^8	0.20	2100	0	40	-
Clay	SB2	$2.4{\cdot}10^7$	0.20	1894	$2.5{\cdot}10^4$	0	$2.5{\cdot}10^4$
Rigid	SB3	-	-	-	-	-	-

For each soil considered, density ρ, cohesion c', internal friction angle, ϕ, elastic modulus, E_{seabed}, and shear strength, S_u, are reported [34]. The yield stresses are defined via a bilinear curve using the following formulation:

$$\tau_f = c' + \sigma_n \cdot \tan\phi \quad (5)$$

It is important to underline the fact that the seabed considered refers to very high-performance soils, as the weight of the overlying water makes them mechanically more resistant. This consideration applies, in general, to all underwater seabed terrains.

A total of 108 cases were simulated, and Table 6 provides an alphanumeric code for each numerical simulation.

As far as fluid domain simulation is concerned, MSC Dytran offers two methods [36]. The first method, called general coupling, can be applied to non-orthogonal Euler meshes, but it is computationally expensive. The second method, which is called fast coupling, requires the Euler mesh to be orthogonal, and it is considerably faster. This makes the fast-coupling approach the most used method. An important step within MSC Dytran is the definition of the coupling surface between the Eulerian and the Lagrangian domains to solve FSI. The coupling surface defines what part of the Eulerian domain is occupied by the structure. Therefore, when a submerged body is considered, the coupling surface must define a closed volume to separate the fluid domain from the structural one. If the object of the investigation is modelled with shell elements, like the considered plates, the coupling surface will no longer act as a container but will only act as a barrier to fluid flow. This approach is called auto-coupling in MSC Dytran. Such a modelling strategy is adopted in the presented study since it is the preferred choice for plates, allowing for a reduction in the number of cells involved in the calculations. A specific FSI algorithm was used by the software to couple both the Lagrangian and Eulerian domains [36,37].

The fluid domain represented by the water underwent discretisation, employing cell-centred finite volumes (CCFVs), which are advantageous for forecasting discontinuities arising from the shock wave. This aligns with the Eulerian formulation, wherein the mesh remained stationary while the fluid traversed through it. The considered fluid domain (Figure 3a) is a box with dimensions 2.7 m × 2.7 m × 2.7 m meshed with a hexahedral cell with a base size of 15 mm. This mesh dimension ensures good accuracy regarding the peak pressure generated by the explosion scenario. At all outer boundaries of the 3-D domain, a flow non-reflecting boundary condition is imposed.

Table 6. Codes for all the cases considered in the dataset.

	Code	Case	Code	Case	Code
1	AL-LC1-R1-SB3	37	AL-LC1-R1-SB2	73	ST-LC1-R1-SB1
2	AL-LC2-R1-SB3	38	AL-LC2-R1-SB2	74	ST-LC2-R1-SB1
3	AL-LC3-R1-SB3	39	AL-LC3-R1-SB2	75	ST-LC3-R1-SB1
4	AL-LC4-R1-SB3	40	AL-LC4-R1-SB2	76	ST-LC4-R1-SB1
5	AL-LC5-R1-SB3	41	AL-LC5-R1-SB2	77	ST-LC5-R1-SB1
6	AL-LC6-R1-SB3	42	AL-LC6-R1-SB2	78	ST-LC6-R1-SB1
7	AL-LC7-R1-SB3	43	AL-LC7-R1-SB2	79	ST-LC7-R1-SB1
8	AL-LC8-R1-SB3	44	AL-LC8-R1-SB2	80	ST-LC8-R1-SB1
9	AL-LC9-R1-SB3	45	AL-LC9-R1-SB2	81	ST-LC9-R1-SB1
10	AL-LC1-R2-SB3	46	AL-LC1-R2-SB2	82	ST-LC1-R2-SB1
11	AL-LC2-R2-SB3	47	AL-LC2-R2-SB2	83	ST-LC2-R2-SB1
12	AL-LC3-R2-SB3	48	AL-LC3-R2-SB2	84	ST-LC3-R2-SB1
13	AL-LC4-R2-SB3	49	AL-LC4-R2-SB2	85	ST-LC4-R2-SB1
14	AL-LC5-R2-SB3	50	AL-LC5-R2-SB2	86	ST-LC5-R2-SB1
15	AL-LC6-R2-SB3	51	AL-LC6-R2-SB2	87	ST-LC6-R2-SB1
16	AL-LC7-R2-SB3	52	AL-LC7-R2-SB2	88	ST-LC7-R2-SB1
17	AL-LC8-R2-SB3	53	AL-LC8-R2-SB2	89	ST-LC8-R2-SB1
18	AL-LC9-R2-SB3	54	AL-LC9-R2-SB2	90	ST-LC9-R2-SB1
19	AL-LC1-R1-SB1	55	ST-LC1-R1-SB3	91	ST-LC1-R1-SB2
20	AL-LC2-R1-SB1	56	ST-LC2-R1-SB3	92	ST-LC2-R1-SB2
21	AL-LC3-R1-SB1	57	ST-LC3-R1-SB3	93	ST-LC3-R1-SB2
22	AL-LC4-R1-SB1	58	ST-LC4-R1-SB3	94	ST-LC4-R1-SB2
23	AL-LC5-R1-SB1	59	ST-LC5-R1-SB3	95	ST-LC5-R1-SB2
24	AL-LC6-R1-SB1	60	ST-LC6-R1-SB3	96	ST-LC6-R1-SB2
25	AL-LC7-R1-SB1	61	ST-LC7-R1-SB3	97	ST-LC7-R1-SB2
26	AL-LC8-R1-SB1	62	ST-LC8-R1-SB3	98	ST-LC8-R1-SB2
27	AL-LC9-R1-SB1	63	ST-LC9-R1-SB3	99	ST-LC9-R1-SB2
28	AL-LC1-R2-SB1	64	ST-LC1-R2-SB3	100	ST-LC1-R2-SB2
29	AL-LC2-R2-SB1	65	ST-LC2-R2-SB3	101	ST-LC2-R2-SB2
30	AL-LC3-R2-SB1	66	ST-LC3-R2-SB3	102	ST-LC3-R2-SB2
31	AL-LC4-R2-SB1	67	ST-LC4-R2-SB3	103	ST-LC4-R2-SB2
32	AL-LC5-R2-SB1	68	ST-LC5-R2-SB3	104	ST-LC5-R2-SB2
33	AL-LC6-R2-SB1	69	ST-LC6-R2-SB3	105	ST-LC6-R2-SB2
34	AL-LC7-R2-SB1	70	ST-LC7-R2-SB3	106	ST-LC7-R2-SB2
35	AL-LC8-R2-SB1	71	ST-LC8-R2-SB3	107	ST-LC8-R2-SB2
36	AL-LC9-R2-SB1	72	ST-LC9-R2-SB3	108	ST-LC9-R2-SB2

To solve the equations of fluid flow, equations of state (EOS) and initial conditions should be implemented for the different portions of the domain [37].

During the underwater explosion, the fluid domain includes two main materials: the explosive (detonation product gases) and water. The Jones-Wilkins-Lee (JWL) EOS is adopted to describe the evolution of the charge explosion, which can be expressed as follows [38]:

$$p = A\cdot(1-\omega/(R_1\cdot V))\cdot e^{-R_1\cdot V} + B\cdot(1-\omega/(R_2\cdot V))\cdot e^{-R_2\cdot V} + \omega\cdot e/V \quad (6)$$

where p, V, and e are the pressure, relative volume, and relative internal energy of the detonation products, respectively. A, B, R_1, R_2, and ω are the adjustable parameters [39].

Finally, polynomial EOS is specified for water. It relates the pressure in the fluid to the acoustic condensation, μ, and the specific internal energy, e. When $\mu > 0$ (compression), we have

$$p = a_1\cdot\mu + a_2\cdot\mu^2 + a_3\cdot\mu^3 + \left(b_0 + b_1\cdot\mu + b_2\cdot\mu^2\right)\cdot\rho_0\cdot e \quad (7)$$

while for $\mu < 0$ (tension), we have

$$p = a_1 \cdot \mu + (b_0 + b_1 \cdot \mu) \cdot \rho_0 \cdot e \quad (8)$$

where p is the pressure, $\mu = \eta - 1$, $\eta = \rho/\rho_0$, ρ_0 is the reference density, ρ is the whole material density, and a_1, a_2, a_3, b_0, b_1, and b_2 are Eulerian fluid constants. Finally, e represents the specific internal energy per unit mass. The constants were obtained by comparing the relevant constants between Equations (7) and (8).

A resume of all Eulerian material properties used in the present simulations, with the related model used in MSC Dytran, is reported in Table 7:

Table 7. Resume of the Eulerian material properties (water, air, and charge) for the experimental validation model.

Material	MSC Dytran Model	Input Parameters
Water	Polynomial equation of state (EOSPOL)	$\rho = 1025$ [kg/m^3], $K = 2.2{\cdot}10^9$ [Pa], $e = 83950$ [J/kg], $a_1 = 2.314{\cdot}10^9$ [Pa], $a_2 = 6.561{\cdot}10^9$ [Pa], $a_3 = 1.126{\cdot}10^9$ [Pa], $b_0 = 0.4934$ [−], $b_1 = 1.3937$ [−], $b_2 = 0.00$ [−]
Charge (TNT)	JWL equation of state (EOSJWL)	$\rho = 1630$ [kg/m^3], $W = 1.47$ [kg], $e = 4.76{\cdot}10^6$ [kJ/kg], $A = 3.7{\cdot}10^{11}$ [−], $B = 2.23{\cdot}10^9$ [−], $R_1 = 4.15$ [−], $R_2 = 0.95$ [−], $\omega = 0.3$ [−]

A total time of 3 ms is considered in all simulations. This period does not induce any effects due to the presence of gas bubbles, and this choice does not affect the machine learning method investigated in the present work, as previously mentioned. Each analysis within the dataset required approximately 36 h for a Lenovo workstation (Lenovo Group Ltd., Beijing, China) with 128 GB of RAM and an Intel® Core™ i9-13900K 3.00 GHz CPU. This amount of time highlights the limit of coupled Eulerian–Lagrangian analysis, especially when thinking about applications for entire ship structures.

2.2. Dataset Generation

The data required for the MLNN is extracted from the numerical simulations using ParaView scripts. The data extracted from each simulation are the following:

- Distance, R (Figure 2), before the explosive event takes place;
- Type of seabed, identified with the E_{seabed} of the material shown in Table 5;
- Material of the plate, identified with the E_{plate} shown in Table 2;
- Initial mass-per-unit-area, m_a, values of the plates calculated according to the following equation:

$$m_a = \rho \cdot s \quad (9)$$

  where ρ is the material density, and s is the plate thickness.
- Position of the charge within the user-defined grid, presented in Figure 2, through the indication of x_{charge} and z_{charge}, as listed in Table 1;
- Pressure-time history $p(t)$ recorded on the central mesh element of the plate (red dot in Figure 2);
- Vertical displacement-time history, $d(t)$, recorded on the central mesh element of the plate (red dot in Figure 2).

The $p(t)$ is further processed to extract the most relevant information: the first peak pressure, $p_{first,peak}$ (direct shock), the second peak pressure, $p_{second,peak}$ (reflected shock),

the time instant when the first peak occurs, $t_{first,peak}$, the time instant when the second peak occurs, $t_{second,peak}$, and finally, the time instant of the first rise in the curve, t_{raise}. The identification of $p_{second,peak}$ and $t_{second,peak}$ is not trivial, so a threshold filter is implemented to obtain both values.

Moreover, for $d(t)$, the most relevant information is extracted, which is the maximum value of vertical displacement at the end of the transient analysis, U_{max}.

Representative extracted features are shown in Figure 4 in reference to simulation AL-LC1-R1-SB3 (Table 6). All inputs have been normalised to ensure that each feature contributed equally to the analysis.

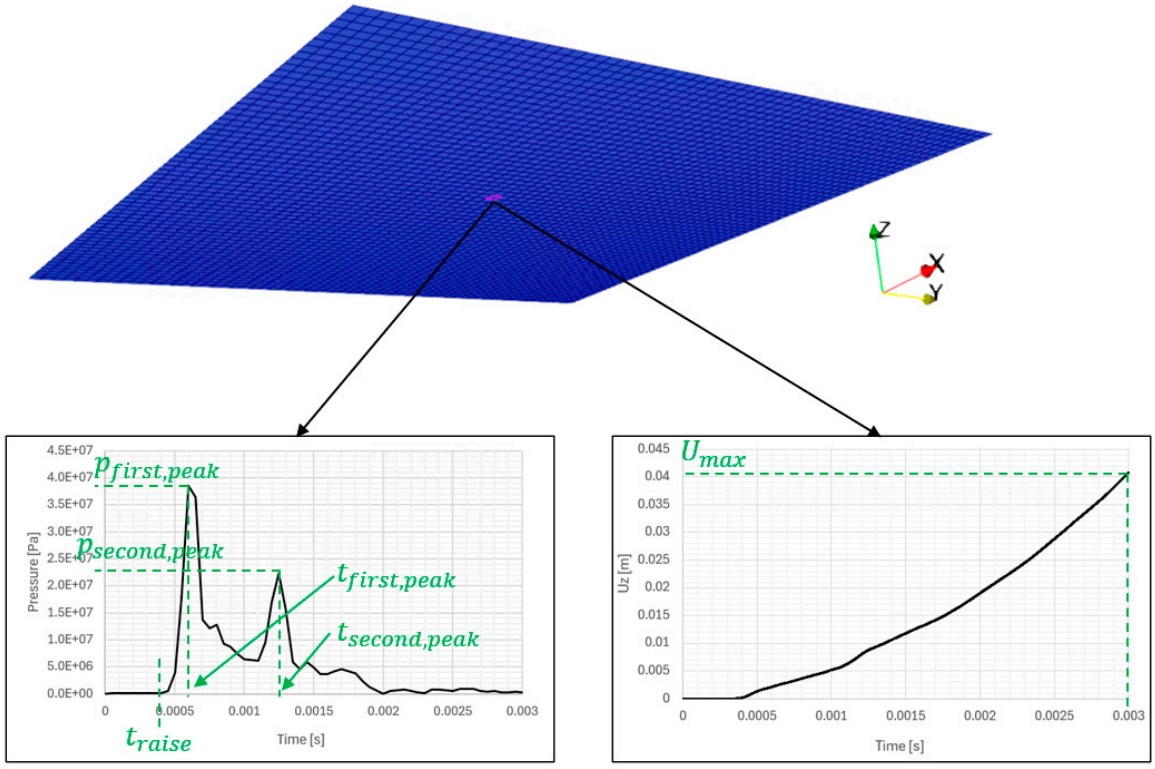

(**a**)

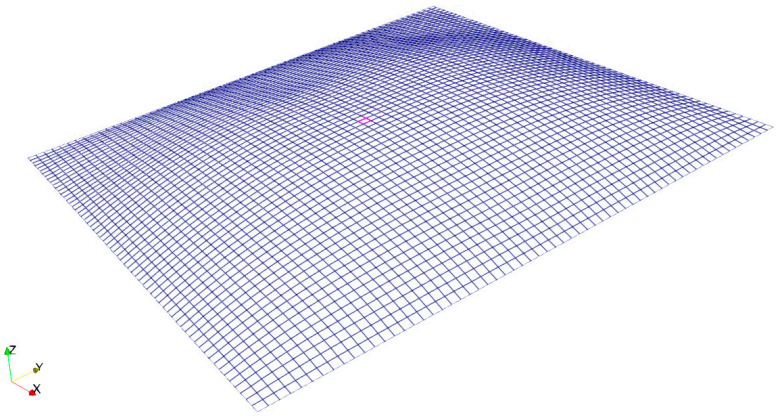

(**b**)

Figure 4. (**a**) Indication of the extraction process for a generic case inside the dataset (AL-LC1-R1-SB3): pressure and vertical displacement pattern for the central mesh element of the plate, and (**b**) qualitative, real-scaled contour plot for the same case at t = 0.003 s (pictures taken using ParaView version 5.12.0).

After some examination, the authors identified that some features are inherently more influential than others in determining the outcome. In particular, $t_{first,peak}$ and U_{max} were

found to be significantly influential. In recognising their importance, the authors modified the sensitivity of the machine learning model with respect to these critical features by multiplying the weights of these two key features by 10. This adjustment makes the neural network more influenced by these two features, improving the accuracy of the predictions.

To be highlighted is the fact that the selected input parameters ensure that different configurations, such as varying charge mass and stand-off distance, do not yield identical input data, allowing the neural network to accurately infer the detonation point location by capturing complex relationships and minimising ambiguity, especially in real-world applications with multiple sensors.

A data augmentation procedure is not exploited in this case study for simplicity. The training data of all 108 cases were randomly divided into two groups, with 80% for training and 20% for validation and testing, as is commonly carried out in neural network applications [36].

It worth noting that for the training and validation steps, x_{charge} and z_{charge} are known, while in a real application, such parameters are unknown and represent the target data to be obtained from the proposed procedure [40]. All the other parameters are known by the ship crew by using specific sensors or calculations.

Table 8 shows some methods that the crew can use in a real application to obtain the information needed for ML procedures to identify the location of the UNDEXs.

Table 8. Examples of research applicable to the present framework to feed the machine learning strategy.

Type of Information	Provided By	References
Displacement history	• Accelerometers, by integration • SHM strategies, like the inverse Finite Element Method	[41–45]
Pressure history	Different types of sensors (FBG, etc.)	[46]
Distance between the hull and seabed	Echo Sounders	[47]
Type of the seabed	Echo Sounders, sonars, underwater drones, etc.	[47]
Material and thickness of the plate	Known from the design phase (Society of Classification rules)	[33]
BCs	Known from the design phase (sub-modelling, etc.)	[33]

2.3. Data-Driven Approach

Given the complexity of the problem and the need for a balance between accuracy and computational efficiency, a feed-forward Multi-Layer Neural Network was decided on as the machine learning model, as it demonstrated superior performance compared to traditional methods, like linear regression and decision trees, while also offering the flexibility to scale effectively with larger datasets and real-world scenarios [27,40].

MLNNs are models commonly employed to approximate linear and/or non-linear functions between input ($\boldsymbol{x}$) and output ($\boldsymbol{y}$) vectors according to the following form:

$$\boldsymbol{y} = f(\boldsymbol{x}) \tag{10}$$

MLNNs consist of interconnected units known as neurons (or nodes), organised into multiple layers: an input layer, one or more hidden layers, and an output layer.

Typically, neurons in consecutive layers are fully connected, meaning that each node in a layer is linked to all the nodes in the subsequent layer.

The i-th component, x_i, of the input vector ($\boldsymbol{x}$) is assigned to the i-th neuron within the input layer, which transfers information to neuron j in the subsequent layer through a

weighted connection characterised by the weight of w_{ij}. The information obtained by the j-th node is then aggregated and updated according to the following equation [36]:

$$z_j = g\left(\sum_{i=1}^{N_j}(w_{ij} \cdot x_i) + b_j\right) \tag{11}$$

where z_j is the output of the j-th node, $g(\cdot)$ is a typically non-linear activation function, N_j represents the number of nodes from which the j-th node receives information, and b_j is a bias parameter. This message-passing and aggregation process recurs layer-by-layer until reaching the output layer, where the value of the k-th node corresponds to the k-th component ($\hat{y}_k$) of the estimated output vector ($\hat{\boldsymbol{y}}$). The weights, w_{ij}, and biases, b_j, are trainable parameters of the MLNN and are optimised during training through error back-propagation algorithms with gradient descent aimed at minimising the discrepancy between the expected output ($\boldsymbol{y}$) and the predicted output ($\hat{\boldsymbol{y}}$).

The training set is used to make the MLNN learn the relationship between inputs and outputs, the validation set serves as a tool to indicate underfitting or overfitting, and the testing set is used after training for evaluating the MLNN generalisation capabilities on unseen data. As usual, a user-defined error metric comparing predicted and expected outputs guides the iterative update of the trainable parameters using gradient descent, culminating in achieving satisfactory reconstruction error [40].

Various MLNN architectures are explored in this work, but for the sake of brevity, only the best-performing configuration is presented in Figure 5 through a schematic diagram. Here, a feed-forward deep neural network (DNN) architecture with a back-propagation algorithm is investigated. This choice is due to the predictive capabilities since this architecture can be faster to train compared to other more complex neural network architectures, such as recurrent neural networks (RNNs) or convolutional neural networks (CNNs), especially with a small dataset [48].

The MLNN is characterised by three fully connected layers: the input layer with data previously discussed, the hidden layers, and the output layer. The number of neurons for each layer decreases to facilitate prediction; the first hidden layer has 64 neurons, the second one has 32 neurons, and the last layer (output) has 9 neurons, one for each possible class, corresponding to a specific detonation point according to the user-defined grid of Figure 2.

Parameter selection for the MLNN model, including the number of hidden layers and neurons, is determined through empirical testing and guidelines available in the literature [40,49], with two hidden layers (64 and 32 neurons, respectively) providing the best balance between complexity and performance without overfitting.

The output class values are represented by 9 binary vectors, thanks to the well-known one-hot encoding technique [50]. By doing so, the neural network can have 9 neurons in the last layer, representing the classification probabilities of each possible outcome.

The ReLU activation function is applied to the input and hidden layers, which ensures non-linearity in the overall system. After the first layer, dropout is applied at a rate of 10%. The dropout function is a regularisation technique used in machine learning, particularly in neural networks, to prevent overfitting. Overfitting occurs when a model learns the training data too well, capturing noise and details that do not generalize to new data. Dropout addresses this by randomly "dropping out" 10% of the units (neurons) in the neural network during training, which forces the model to learn more robust features [51]. The SoftMax activation function [40] is used for the output layer since it ensures that the sum of the probabilities for all classes equals 1. The output values from the SoftMax function can be interpreted directly as probabilities. This is useful for model interpretation and decision-making, as the user can see how confident the model is in its predictions for each class.

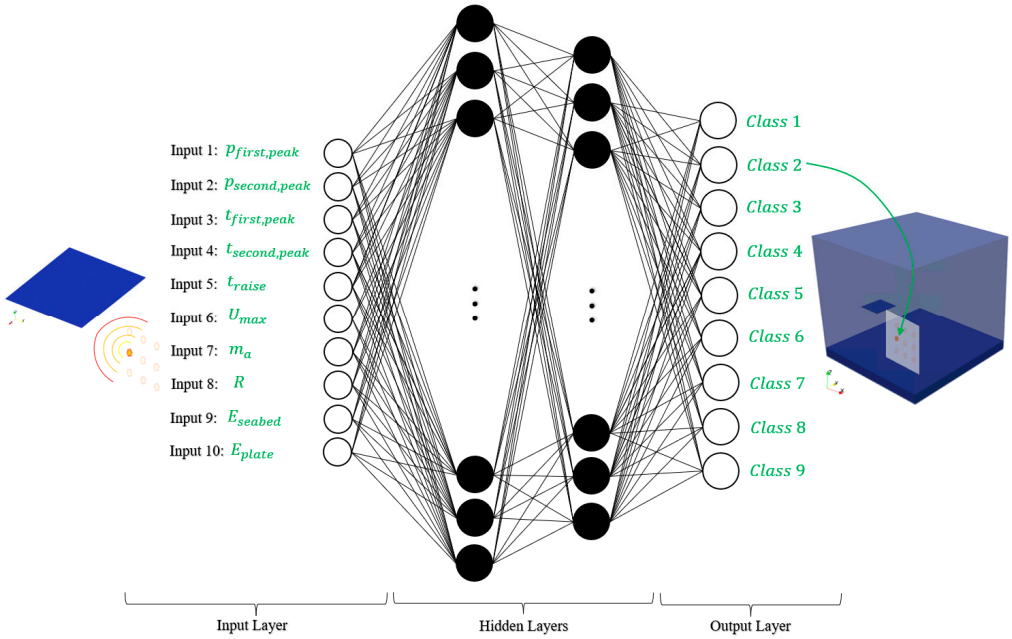

Figure 5. Schematic diagram of the MLNN model of the present framework.

Training was performed using the Adam optimiser [52], and a total number of 1000 epochs were set up, in which neurons change their weights to try to optimize the classification function. A cross-entropy loss function was employed since it is widely used in multi-class classification problems.

Metrics are tracked during the training process, with an early stopping criterion set to trigger if the validation loss does not decrease for 30 consecutive epochs. Training is terminated either according to the early stopping criterion or, in particular, when the model weights are reverted to those from the epoch that had the best validation loss within the last 30 epochs. This strategy allows for not wasting unnecessary time by terminating all 1000 epochs if not necessary. The learning rate starts from 0.01 and regresses by 1/10 to two predetermined milestone epochs, which correspond to epoch 400 and epoch 800, to find the best fitting solution.

Batch size represents the number of samples provided as input for each epoch, which are processed simultaneously by the network. Normally, a fairly large number is chosen for the batch size, such as 64; however, in the present case, with a small dataset available, the authors found that the right compromise was to set the batch size to 16.

3. Results and Discussion

An example of the results of a representative numerical analysis inside the dataset, regarding the AL-LC1-R1-SB3 case of Table 6, is shown in Figure 6. Here, the pressure and density contour field are depicted, and, to have a better view, a vertical section of the Eulerian domain was made, but not for the structure and seabed. All other analyses in the dataset have the same pattern (qualitatively), with the differences in the values shown (e.g., a charge farther away from the plate will have lower pressures recorded on the surface of the plate and will arrive later than a charge closer to it). As shown, the structure is subjected to a double hit: initially, it is hit by the direct shock caused by the explosion, and in the subsequent moments, the reflected wave induced by the seabed is present. This double hit is revealed by the pressure trend recorded at the point of investigation in the plate and is a very important feature that will be used by the network to learn where the explosion departed.

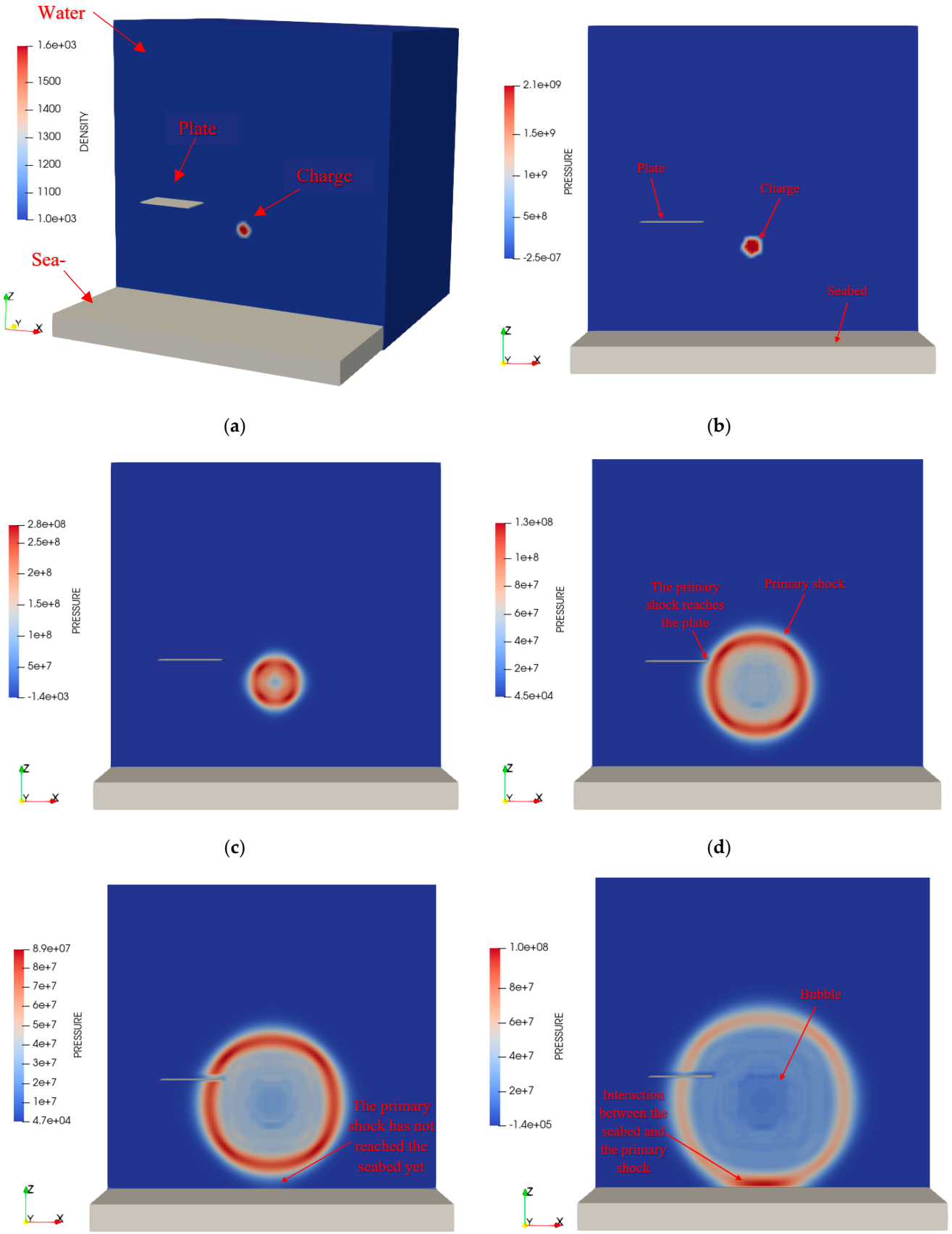

Figure 6. *Cont.*

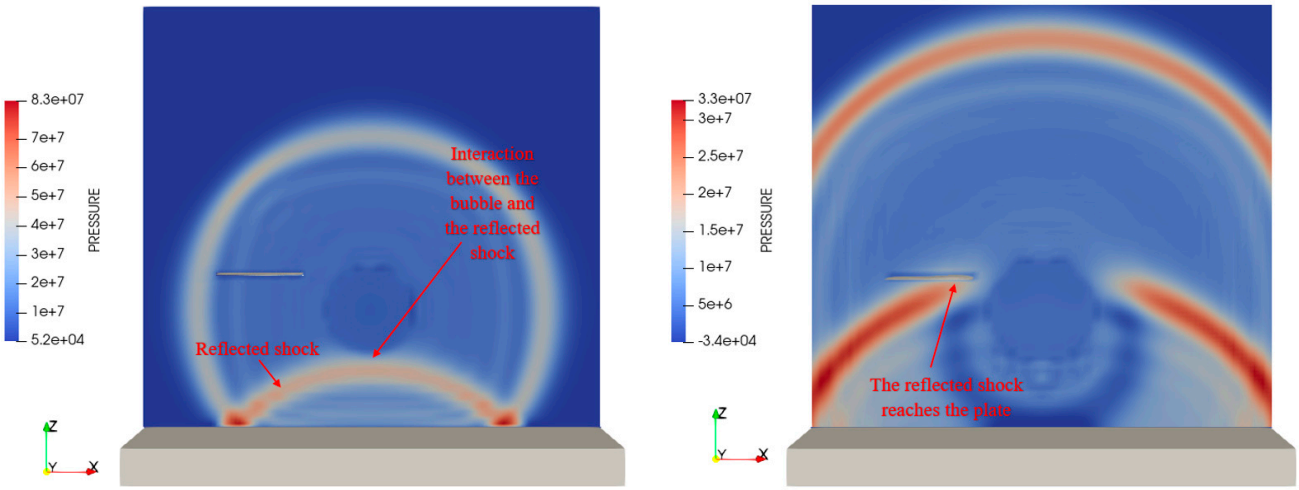

(**g**) (**h**)

Figure 6. Pressure and density field at different instants for the 3-D model: (**a**) density (kg/m^3) at t = 10^{-8} s, (**b**) pressure (Pa) at t = 0.00010 s, (**c**) pressure (Pa) at t = 0.00025 s, (**d**) pressure (Pa) at t = 0.00035 s, (**e**) pressure (Pa) at t = 0.00035 s, (**f**) pressure (Pa) at t = 0.00045 s, (**g**) pressure (MPa) at t = 0.00070 s, and (**h**) pressure (MPa) at t = 0.00110 s (pictures taken using ParaView, with the legend limits rescaled to provide a better view of the shocks).

The authors verified the accuracy of the numerical results in Figure 6 by comparing the recorded numerical peak pressure with the analytical formulas available in the literature. In particular, the formulation proposed by Cole was employed [11]. It should be noted, however, that this formula can be applied to any charge size, from a few grains to nuclear weapons, detonated at any depth; it describes the shock wave accurately except in the immediate vicinity of the explosive charge (within 10 times the charge radius R_{charge}), where the peak pressure is higher than the one predicted by the formula. Additionally, it should be noted that the formulation is valid in the free-field case, and it is specific to TNT charges. The formulations used are the following:

$$p(t) = P_m \cdot e^{-t/\theta} \tag{12}$$

$$P_m = 52.16 \cdot \left(\frac{W^{1/3}}{S}\right)^{1.13} \tag{13}$$

$$\vartheta = 96.5 \cdot W^{1/3} \cdot \left(\frac{W^{1/3}}{S}\right)^{-0.22} \tag{14}$$

where $p(t)$ is the pressure-time history at a fixed location, P_m is the peak pressure in MPa, t is the time, θ is the decay time in microseconds, W is the equivalent TNT mass in kg, and finally, S is the stand-off distance in meters. We refer the reader to [46] for more details about the formulation and coefficients. Three different points of the water domain were considered for the verification of the pressure trend and pressure peaks. These probe points are shown in Figure 7a, and they belong to the vertical plane that intersects the centre of the charge. Figure 7a also shows a red circle, which outlines the validity domain of the previous formulations (scenario AL-LC1-R1-SB3 of Table 6); Figure 7b shows the comparison between the numerical and analytical pressure-time histories.

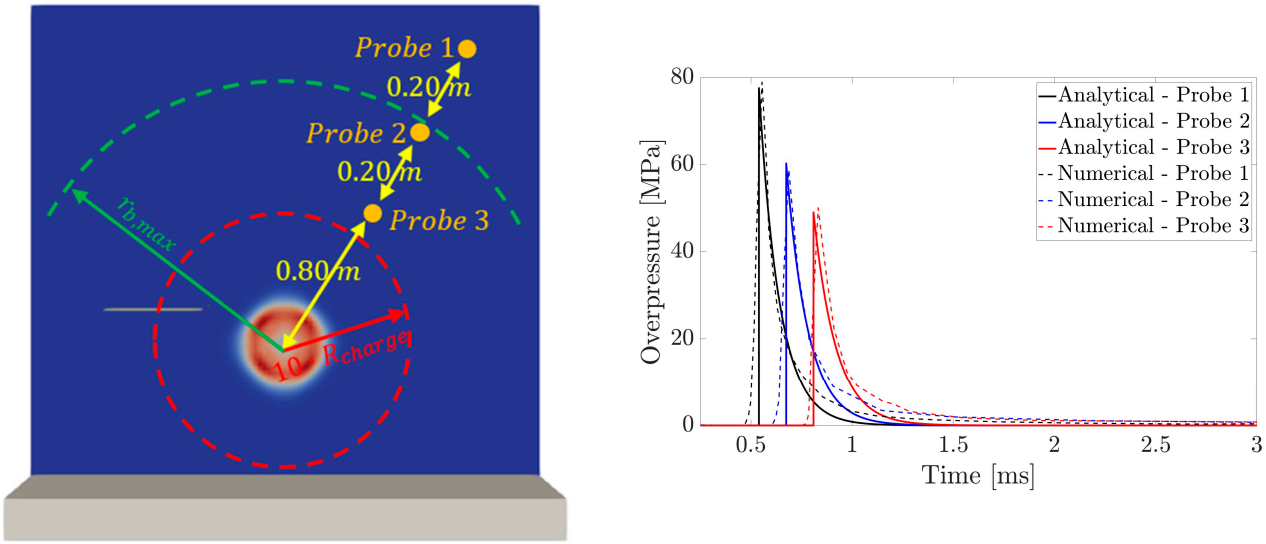

(**a**) (**b**)

Figure 7. (**a**) Indication of the probe locations for the validation of the pressure-time trends, and (**b**) a comparison between the numerical and analytical pressure trends.

The performance of the MLNN over the cases within the test set of Table 1 is presented through the following metrics, which are commonly used for classification problems. The macro-averaging technique is applied to condense the calculated metrics for each class into a single global metric.

- Accuracy (proportion of correct predictions (both true positives and true negatives) out of the total number of predictions made) equal to 99.09;
- Precision (proportion of correctly predicted positive observations to the total predicted positives) equal to 99.25;
- Recall (proportion of correctly predicted positive observations to all observations in the actual positive class) equal to 99.55;
- F1 score (harmonic mean of precision and recall) equal to 99.16;
- Confusion matrix (the number of correct and incorrect predictions broken down by each class); visible in Figure 8a.

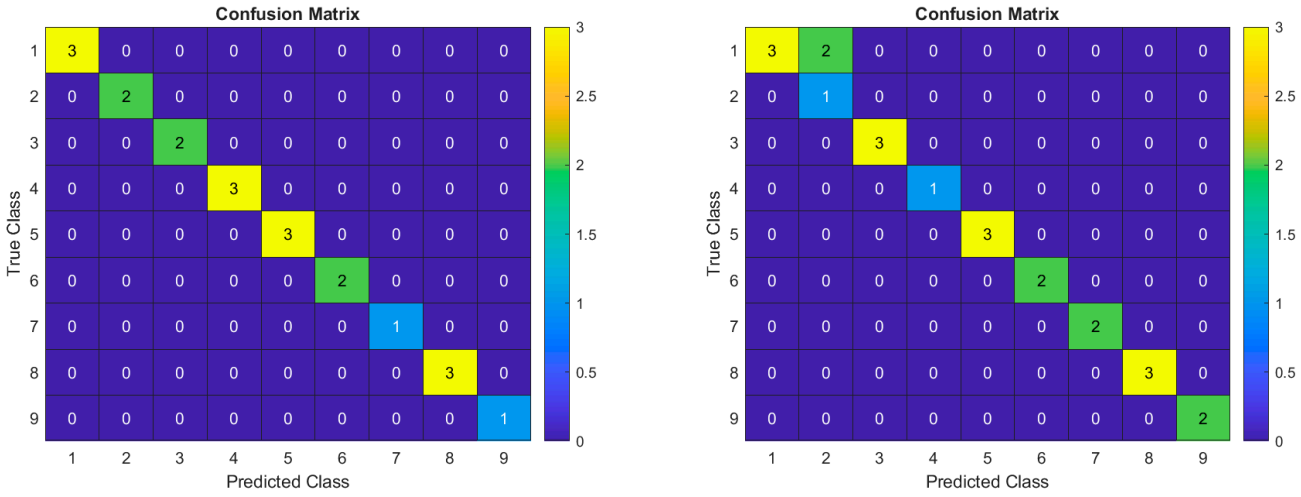

(**a**) (**b**)

Figure 8. Confusion matrix for two different sets of training, validation, and test sets: (**a**) without misclassification; (**b**) with two misclassifications.

Regarding all the previous metrics, the results provide evidence that the network successfully learned how to associate the inputs to the correct class. In other words, the MLNN correctly predicts the position of the detonation point of the explosive events in all cases within the test set. As shown in Figure 8a, the off-diagonal elements of the confusion matrix are all zeros, indicating that there are no misclassifications for all cases belonging to the test samples randomly chosen during the split procedure of the dataset. The predictions presented in Figure 8a are resumed in Table 9.

Table 9. Prediction for the cases considered in the test set of Figure 8a.

	Code	Actual Class (x_{charge} [m], z_{charge} [m])	Predicted Class (x_{charge} [m], z_{charge} [m])
1	AL-LC1-R1-SB1	1 (0.65, 0.20)	1 (0.65, 0.20)
2	AL-LC1-R2-SB3	1 (0.65, 0.20)	1 (0.65, 0.20)
3	ST-LC1-R1-SB1	1 (0.65, 0.20)	1 (0.65, 0.20)
4	AL-LC2-R2-SB1	2 (0.85, 0.20)	2 (0.85, 0.20)
5	ST-LC2-R2-SB3	2 (0.85, 0.20)	2 (0.85, 0.20)
6	ST-LC3-R2-SB2	3 (1.05, 0.20)	3 (1.05, 0.20)
7	AL-LC3-R1-SB3	3 (1.05, 0.20)	3 (1.05, 0.20)
8	ST-LC4-R1-SB2	4 (0.85, 0.20)	4 (0.85, 0.20)
9	AL-LC4-R1-SB1	4 (0.85, 0.20)	4 (0.85, 0.20)
10	ST-LC4-R2-SB2	4 (0.85, 0.20)	4 (0.85, 0.20)
11	AL-LC5-R2-SB1	5 (0.85, 0.40)	5 (0.85, 0.40)
12	ST-LC5-R2-SB3	5 (0.85, 0.40)	5 (0.85, 0.40)
13	AL-LC5-R2-SB2	3 (1.05, 0.20)	5 (0.85, 0.40)
14	ST-LC6-R2-SB2	6 (0.85, 0.60)	6 (0.85, 0.60)
15	ST-LC6-R1-SB1	6 (0.85, 0.60)	6 (0.85, 0.60)
16	ST-LC7-R1-SB1	7 (1.05, 0.20)	7 (1.05, 0.20)
17	ST-LC8-R2-SB1	8 (1.05, 0.40)	8 (1.05, 0.40)
18	AL-LC8-R1-SB1	8 (1.05, 0.40)	8 (1.05, 0.40)
19	AL-LC8-R1-SB3	8 (1.05, 0.40)	8 (1.05, 0.40)
20	AL-LC9-R2-SB2	9 (1.05, 0.60)	9 (1.05, 0.60)

The authors point out that the choice of the number of numerical simulations is because testing with 90, 100, and 108 cases did not show significant improvements in performance beyond 90 simulations due to the careful selection of features that allowed the network to effectively learn the input-output relationships. As a result, it was not necessary to increase the dataset further.

Neural networks are highly sensitive to the choice of training, validation, and test splits, especially for very small datasets, where the risk of overfitting or underfitting due to improper data partitioning is significantly higher [25,40]. Additional investigations were performed by the authors to check the sensitivity of the present architecture to the random split of the dataset. A total of 100 trials were tested, where the training, validation, and test sets were continuously changed at each trial. For the 90% cases, the metrics are accurate and reliable, as per those presented in Figure 8a. The results for the remaining 10% are still accurate since a maximum of two misclassifications were revealed. An example of this is shown in Figure 8b, where the representative matrix contains two errors, specifically two misclassifications of class 1 as class 2.

To further support the results presented in Figure 8, Figure 9 illustrates the evolution of the cross-entropy loss for both the training and validation sets as a function of the number of epochs. The plot confirms that the model successfully converges, with both losses decreasing smoothly and stabilising after approximately 20 epochs. Although minor fluctuations are observed beyond this point, particularly in the validation loss, they remain

within an acceptable range, indicating that the model does not suffer from overfitting. This further validates the robustness and generalisation capability of the trained network.

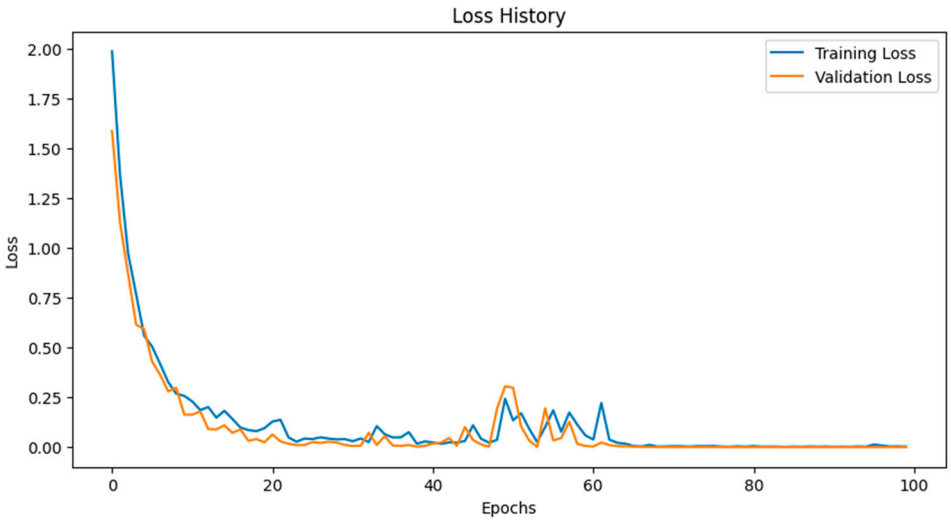

Figure 9. The plot of cross-entropy loss as a function of epoch number.

In conclusion, the presented results demonstrate the high accuracy of the proposed model across different test data, as evidenced by an accuracy of 99.09%, a precision of 99.25%, a recall of 99.55%, and an F1-score of 99.16%. These metrics confirm the effectiveness of the classification approach for this dataset despite the limited number of simulations.

A crucial point of the present framework lies in the main limitation of being able to identify the position of the detonation point of an underwater explosive based on the nodes of a two-dimensional grid. The authors carried out further investigations to understand what the predicted class would be, i.e., the location of the detonation point, in cases where the explosive detonates in points other than those of the grid. The new analysis carried out for this check is visually reported in Figure 10 and described in detail in Tables 10 and 11 (the "N" in front of the new load codes refers to "New"). What emerged is that the network can provide the class in the output corresponding to the closest point of the grid of new cases (based on Euclidian's distance), showing excellent generalisation capabilities.

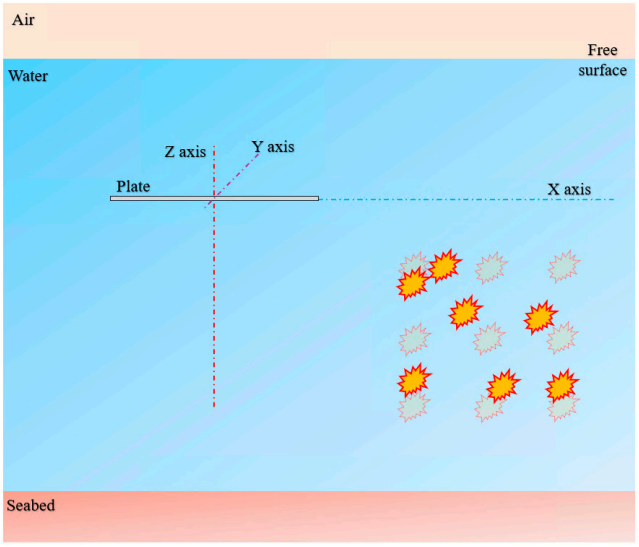

Figure 10. Indication of the new detonation points used to investigate the generalisation capabilities of the MLNN.

Table 10. Codes for the new scenarios considered.

	Code		Code
1	AL-NLC1-R1-SB3	6	ST-NLC2-R2-SB2
2	AL-NLC3-R2-SB1	7	ST-NLC4-R1-SB3
3	AL-NLC5-R1-SB2	8	ST-NLC6-R2-SB1
4	AL-NLC7-R2-SB2	9	ST-NLC8-R1-SB2
5	AL-NLC9-R1-SB1	10	ST-NLC10-R2-SB1

Table 11. Features of the new explosion scenarios considered.

Code	Charge	m [kg]	EOS	R_{charge} [m]	x_{charge} [m]	z_{charge} [m]
NLC1	TNT	1.47	JWL	0.060	0.72	0.20
NLC2	TNT	1.47	JWL	0.060	0.72	0.20
NLC3	TNT	1.47	JWL	0.060	0.65	0.26
NLC4	TNT	1.47	JWL	0.060	0.82	0.37
NLC5	TNT	1.47	JWL	0.060	0.82	0.37
NLC6	TNT	1.47	JWL	0.060	1.02	0.37
NLC7	TNT	1.47	JWL	0.060	0.65	0.56
NLC8	TNT	1.47	JWL	0.060	0.87	0.54
NLC9	TNT	1.47	JWL	0.060	1.05	0.54
NLC10	TNT	1.47	JWL	0.060	1.05	0.54

In many practical scenarios, such as naval operations, pinpoint accuracy at the millimetre level is not always necessary for reconstructing the detonation point of a generic underwater threat. Instead, a lower resolution is often sufficient to achieve the objectives of the analysis. For example, understanding whether an explosion occurred within a 1 m or 2 m grid area is generally adequate for making informed decisions about response and impact assessment. High-resolution data may provide excessive detail that does not significantly alter operational decisions or resource allocation, and a coarser resolution still offers a clear understanding of the explosion's general location and effects, allowing for more efficient and practical decision-making.

4. Conclusions

This work introduces a novel approach using numerical simulations and a Multi-Layer Neural Network to accurately pinpoint the detonation point of contact of underwater explosions against horizontal, fully clamped underwater plates. The MLNN learns how to correlate inputs from numerical coupled simulations with a specific output class, considering that each class represents a specific position of a detonation point in a bidimensional user-defined grid.

The authors considered that the following inputs were relevant for the framework: the distance between the mid-surface of the plate and seabed, the type of seabed, the material of the plates, the initial mass-per-unit-area, and the pressure and vertical displacement-time history recorded on the central mesh element of the plate. The choice of the previous input data is related to the fact that such information can be obtained by the crew through onboard sensors or instrumentations, allowing for the development of a machine learning tool ready for practical marine structure applications.

The MLNN model was trained using data obtained from a comprehensive finite element (FE) model developed using MSC Dytran software [36]. A total of 108 numerical simulations were generated, including all possible combinations of plate material, type of seabed, and distance between the plate and seabed.

The results show the model's high effectiveness on various test data despite the limited number of simulations. The proof of the performance is based on different common metrics related to classification problems, like accuracy, precision, recall, F1 score, and finally, the well-known confusion matrix.

The primary limitation of the proposed framework is that it can only identify the detonation point of an underwater explosive based on the nodes of a two-dimensional grid. The authors further investigated how the network would predict the location of points not on the grid. The new analysis carried out showed that the network successfully identified the closest grid point based on Euclidean distance, demonstrating excellent generalisation capabilities in an extended application. In practical applications, such as naval operations, pinpoint accuracy at the millimetre level is often unnecessary; instead, a lower resolution, such as determining whether an explosion occurred within a 1 m or 2 m grid area, is generally sufficient for effective decision-making and impact assessment.

Further developments of the present framework include the following aspects:

- Given that the internal behaviour of the present MLNN is not directly accessible without an explainability algorithm, an explainability code should be implemented in the future to elucidate the network and highlight the parameters that influence the MLNN prediction process, with the aim of reducing the input parameter to the most effective setting.
- Gas bubble pulsation and migration against the structure were not considered for the present investigation due to the limited time considered for each numerical simulation. Future developments by the authors will be focused on these aspects since they are the next step in the implementation of the present framework.
- Another improvement for the current framework involves applying it to scenarios where the structure exhibits damage or failure. In such cases, it would be necessary to increase the number of input parameters and account for the mass-per-unit-area variable.
- The present investigation is referred to as a bidimensional user-defined grid (for simplicity) with a certain interspace between the nodes where the charge explodes. In real applications, a three-dimensional aspect should be implemented due to the complexity of the geometry of ships. This aspect significantly increases all the computational efforts required to create a huge database for the machine learning tool.
- A further improvement regarding the present MLNN is represented by its capability to predict both the detonation point and the mass of the charge. The latter quantity will be addressed by the authors in future investigations by exploiting the tool presented here through transfer learning strategies.

Overall, it was found that the MLNN has the great advantage of being accurate and rapid when predicting a detonation point of contact in underwater explosions against metallic plates, starting from a known or calculable (by the crew) input and considering the extremely complex fluid–structure coupling UNDEX effects, as well as geometric and material non-linearities.

Author Contributions: J.B.: Conceptualisation, Methodology, Validation, Formal Analysis, Investigation, Data curation, Writing—original draft preparation, Writing—review and editing, Visualisation. G.K.O.D.: Conceptualisation, Methodology, Validation, Formal Analysis, Investigation, Data curation, Writing—original draft preparation, Writing—review and editing. C.S.: Methodology, Resources, Writing—review and editing, Supervision. A.M.: Conceptualisation, Methodology, Resources, Writing—review and editing, Supervision. All authors have read and agreed to the published version of the manuscript.

Funding: This research received no external funding.

Institutional Review Board Statement: Not applicable.

Informed Consent Statement: Not applicable.

Data Availability Statement: The data given in this article and the data supporting the results of this study are available upon request.

Conflicts of Interest: The authors declared no potential conflicts of interest with respect to the research, authorship, and/or publication of this article.

References

1. Bardiani, J.; Sbarufatti, C.; Manes, A. Transfer Learning with Deep Neural Network Toward the Prediction of the Mass of the Charge in Underwater Explosion Events. *J. Mar. Sci. Eng.* **2025**, *13*, 190. [CrossRef]
2. Bardiani, J.; Lomazzi, L.; Sbarufatti, C.; Manes, A. A Machine Learning-Based Tool to Correlate Coupled and Uncoupled Numerical Simulations for Submerged Plates Subjected to Underwater Explosions. *J. Mar. Sci. Appl.* **2025**, *24*, 1–20. [CrossRef]
3. Bardiani, J.; Giglio, M.; Sbarufatti, C.; Manes, A. On the Exploration of the Influence of Seabed Reflected Waves on Naval Structures. *Eng. Proc.* **2025**, *85*, 7. [CrossRef]
4. de Camargo, F.V. Survey on experimental and numerical approaches to model underwater explosions. *J. Mar. Sci. Eng.* **2019**, *7*, 15. [CrossRef]
5. Tran, P.; Wu, C.; Saleh, M.; Neto, L.B.; Nguyen-Xuan, H.; Ferreira, A.J.M. Composite structures subjected to underwater explosive loadings: A comprehensive review. *Compos. Struct.* **2021**, *263*, 113684. [CrossRef]
6. Zhang, Z.F.; Wang, C.; Wang, L.K.; Zhang, A.M.; Silberschmidt, V.V. Underwater explosion of cylindrical charge near plates: Analysis of pressure characteristics and cavitation effects. *Int. J. Impact. Eng.* **2018**, *121*, 91–105. [CrossRef]
7. Liu, W.T.; Ming, F.R.; Zhang, A.M.; Miao, X.H.; Liu, Y.L. Continuous simulation of the whole process of underwater explosion based on Eulerian finite element approach. *Appl. Ocean. Res.* **2018**, *80*, 125–135. [CrossRef]
8. Peng, Y.-X.; Zhang, A.-M.; Ming, F.-R. Numerical simulation of structural damage subjected to the near-field underwater explosion based on SPH and RKPM. *Ocean. Eng.* **2021**, *222*, 108576. [CrossRef]
9. Ren, S.F.; Zhao, P.F.; Wang, S.P.; Liu, Y.Z. Damage prediction of stiffened plates subjected to underwater contact explosion using the machine learning-based method. *Ocean. Eng.* **2022**, *266*, 112839. [CrossRef]
10. Sagar, H.J.; El Moctar, O. Dynamics of a cavitation bubble between oblique plates. *Phys. Fluids* **2023**, *35*, 013324. [CrossRef]
11. Cole, R.H.; Weller, R. Underwater Explosions. *Phys. Today* **1948**, *1*, 35. [CrossRef]
12. Ming, F.R.; Zhang, A.M.; Xue, Y.Z.; Wang, S.P. Damage characteristics of ship structures subjected to shockwaves of underwater contact explosions. *Ocean. Eng.* **2016**, *117*, 359–382. [CrossRef]
13. Qiankun, J.; Gangyi, D. A finite element analysis of ship sections subjected to underwater explosion. *Int. J. Impact. Eng.* **2011**, *38*, 558–566. [CrossRef]
14. Biglarkhani, M.; Sadeghi, K. Incremental explosive analysis and its application to performance-based assessment of stiffened and unstiffened cylindrical shells subjected to underwater explosion. *Shock. Vib.* **2017**, *2017*, 3754510. [CrossRef]
15. Cui, P.; Zhang, A.M.; Wang, S.P. Small-charge underwater explosion bubble experiments under various boundary conditions. *Phys. Fluids* **2016**, *28*, 117103. [CrossRef]
16. Yu, J.; Liu, J.-H.; Wang, H.-K.; Wang, J.; Zhou, Z.-T.; Mao, H.-B. Application of two-phase transition model in underwater explosion cavitation based on compressible multiphase flows. *AIP Adv.* **2022**, *12*, 025209. [CrossRef]
17. Liu, Y.Z.; Ren, S.F.; Zhao, P.F. Application of the deep neural network to predict dynamic responses of stiffened plates subjected to near-field underwater explosion. *Ocean Eng.* **2022**, *247*, 110537. [CrossRef]
18. Löhner, R.; Li, L.; Soto, O.A.; Baum, J.D. An arbitrary Lagrangian–Eulerian method for fluid–structure interactions due to underwater explosions. *Int. J. Numer. Methods Heat Fluid Flow* **2023**, *33*, 2308–2349. [CrossRef]
19. Ge, L.; Zhang, A.M.; Wang, S.P. Investigation of underwater explosion near composite structures using a combined RKDG-FEM approach. *J. Comput. Phys.* **2019**, *404*, 109113. [CrossRef]
20. Kong, X.S.; Gao, H.; Jin, Z.; Zheng, C.; Wang, Y. Predictions of the responses of stiffened plates subjected to underwater explosion based on machine learning. *Ocean. Eng.* **2023**, *283*, 115216. [CrossRef]
21. Giuliano, D.; Lomazzi, L.; Giglio, M.; Manes, A. On Eulerian-Lagrangian methods to investigate the blast response of composite plates. *Int. J. Impact. Eng.* **2023**, *173*, 104469. [CrossRef]
22. Sigrist, J.F.; Broc, D. A versatile method to calculate the response of equipment mounted on ship hulls subjected to underwater shock waves. *Finite Elem. Anal. Des.* **2023**, *218*, 103917. [CrossRef]
23. Pishevar, A.R.; Amirifar, R. An adaptive ALE method for underwater explosion simulations including cavitation. *Shock Waves* **2010**, *20*, 425–439. [CrossRef]

24. Rackwitz, F. Possibilities and Limitations of ALE Large Deformations Analyses in Geotechnical Engineering. In *Recent Developments of Soil Mechanics and Geotechnics in Theory and Practice*; Triantafyllidis, T., Ed.; Springer International Publishing: Cham, Switzerland, 2020; pp. 97–112. [CrossRef]
25. Nayak, S.; Lyngdoh, G.A.; Shukla, A.; Das, S. Predicting the near field underwater explosion response of coated composite cylinders using multiscale simulations, experiments, and machine learning. *Compos. Struct.* **2022**, *283*, 115157. [CrossRef]
26. Nguyen, G.; Dlugolinsky, S.; Bobák, M.; Tran, V.; García, Á.L.; Heredia, I.; Malík, P.; Hluchý, L. Machine Learning and Deep Learning frameworks and libraries for large-scale data mining: A survey. *Artif. Intell. Rev.* **2019**, *52*, 77–124. [CrossRef]
27. Wang, H.; Liu, B.; Lei, J.; Zhao, N. Improved deep neural network for predicting structural response of stiffened cylindrical shells to far-field underwater explosion. *Ocean. Eng.* **2024**, *298*, 117258. [CrossRef]
28. Ramajeyathilagam, K.; Vendhan, C.P. Deformation and rupture of thin rectangular plates subjected to underwater shock. *Int. J. Impact. Eng.* **2004**, *30*, 699–719. [CrossRef]
29. Moreland, K. *The Paraview Tutorial*; Sandia National Laboratories, Tech. Rep. SAND: Albuquerque, NM, USA, 2013.
30. Gupta, N.K. Response of thin walled metallic structures to underwater explosion: A review. *Int. J. Impact Eng.* **2021**, *156*, 103950. [CrossRef]
31. Hu, H.-W.; Song, P.; Guo, S.-F.; Feng, H.-Y.; Li, D.-K. Shock wave and bubble characteristics of underwater array explosion of charges. *Def. Technol.* **2022**, *18*, 1445–1453. [CrossRef]
32. Costanzo, F.A. Underwater explosion phenomena and shock physics. In *Conference Proceedings of the Society for Experimental Mechanics Series*; Springer: New York, NY, USA, 2011; pp. 917–938. [CrossRef]
33. Jacopo, B. *ShipRight Design and Construction Structural Design Assessment Procedure for Primary Structure of Passenger Ships Working Together for a Safer World*; Lloyd's Register: London, UK, 2004.
34. Dołżyk, K. The Non-Linear Mohr–Coulomb Model for Sands. *Stud. Geotech. Et Mech.* **2006**, *28*, 89–95.
35. Song, C.Y. Fluid–Structure Interaction Analysis and Verification Test for Soil Penetration to Determine the Burial Depth of Subsea HVDC Cable. *J. Mar. Sci. Eng.* **2022**, *10*, 1453. [CrossRef]
36. The MacNeal-Schwendler Corporation. *MSC/DYTRAN User Manual*; MacNeal-Schwendler Corporation: Newport Beach, CA, USA, 2023.
37. Liu, Y.; Li, Z.; Sun, Q.; Fan, X.; Wang, W. Separation dynamics of large-scale fairing section: A fluid-structure interaction study. *Proc. Inst. Mech. Eng. G J. Aerosp. Eng.* **2013**, *227*, 1767–1779. [CrossRef]
38. Shehu, E.; Lomazzi, L.; Giglio, M.; Manes, A. Computational modeling of confined blast waves with focus on interaction with structures. *IOP Conf. Ser. Mater. Sci. Eng.* **2023**, *1275*, 012028. [CrossRef]
39. Koli, S.; Chellapandi, P.; Rao, L.B.; Sawant, A. Study on JWL equation of state for the numerical simulation of near-field and far-field effects in underwater explosion scenario. *Eng. Sci. Technol. Int. J.* **2020**, *23*, 758–768. [CrossRef]
40. Zhou, Z.H. *Machine Learning*; Springer Nature: Cham, Switzerland, 2021. [CrossRef]
41. Varanis, M.; Silva, A.; Mereles, A.; Pederiva, R. MEMS accelerometers for mechanical vibrations analysis: A comprehensive review with applications. *J. Braz. Soc. Mech. Sci. Eng.* **2018**, *40*, 527. [CrossRef]
42. Kefal, A.; Oterkus, E. Displacement and stress monitoring of a Panamax containership using inverse finite element method. *Ocean. Eng.* **2016**, *119*, 16–29. [CrossRef]
43. Bardiani, J.; Manes, A.; Giglio, M.; Sbarufatti, C. Shape Sensing and Damage Identification with iFEM on a Double Bottom Structure of a Containership. In *Latest Advancements in Mechanical Engineering*; Concli, F., Maccioni, L., Vidoni, R., Matt, D.T., Eds.; Springer Nature: Cham, Switzerland, 2024; pp. 225–235. [CrossRef]
44. Bardiani, J.; Giglio, M.; Manes, A.; Sbarufatti, C. Shape sensing with iFEM on a type IV pressure vessel based on experimental measurements. In Proceedings of the 10th EuropeanWorkshop on Structural Health Monitoring (EWSHM 2024), Potsdam, Germany, 10–13 June 2024; Volume 29. [CrossRef]
45. Bardiani, J.; Oppezzo, C.; Manes, A.; Sbarufatti, C. An Inverse FEM for Structural Health Monitoring of a Containership: Sensor Network Optimization for Accurate Displacement, Strain, and Internal Force Reconstruction. *Sensors* **2025**, *25*, 276. [CrossRef]
46. Fukushima, H.; Wakahara, M.; Kanai, T. Hull Surface Pressure Measurement of the Affix-Type Multipoint Pressure Sensor Using Fiber Bragg Gratings. In *Practical Design of Ships and Other Floating Structures*; Okada, T., Suzuki, K., Kawamura, Y., Eds.; Springer: Singapore, 2021; pp. 368–383.
47. Calder, B.R.; Mayer, L.A. Automatic processing of high-rate, high-density multibeam echosounder data, Geochemistry, Geophysics. *Geosystems* **2003**, *4*. [CrossRef]
48. Bengio, Y.; Courville, A.; Vincent, P. Representation Learning: A Review and New Perspectives. *arXiv* **2012**, arXiv:1206.5538. [CrossRef]
49. LeCun, Y.; Bengio, Y.; Hinton, G. Deep learning. *Nature* **2015**, *521*, 436–444. [CrossRef]
50. Pan, H.; Ye, Z.; He, Q.; Yan, C.; Yuan, J.; Lai, X.; Su, J.; Li, R. Discrete Missing Data Imputation Using Multilayer Perceptron and Momentum Gradient Descent. *Sensors* **2022**, *22*, 5645. [CrossRef]

51. Srivastava, N.; Hinton, G.; Krizhevsky, A.; Salakhutdinov, R. Dropout: A Simple Way to Prevent Neural Networks from Overfitting. *J. Mach. Learn. Res.* **2014**, *15*, 1929–1958.
52. Kohli, H.; Agarwal, J.; Kumar, M. An improved method for text detection using Adam optimization algorithm. *Glob. Transit. Proc.* **2022**, *3*, 230–234. [CrossRef]